Remote Sensing of Environment 338 (2026) 115367

Contents lists available at ScienceDirect

Remote Sensing of Environment

journal homepage: www.elsevier.com/locate/rse

Predicting surface soil moisture of northern peatlands from hyper- and multispectral satellite data

Susanna Karlqvist [a,*], Hermanni Aaltonen [b], Mika Aurela [b], Iuliia Burdun [a,c], Mika Korkiakoski [b], Erik Lundin [d], Matthias Peichl [e], Sini-Selina Salko [a], Eeva-Stiina Tuittila [f], Miina Rautiainen [a]

[a] School of Engineering, Aalto University, P.O. Box 14100, FI-00076 Aalto, Finland
[b] Finnish Meteorological Institute, Climate System Research, P. O. Box 503, 00101 Helsinki, Finland
[c] Department of Earth and Environmental Sciences, KU Leuven, Heverlee, Belgium
[d] Abisko Scientific Research Station, Swedish Polar Research Secretariat, Vetenskapens väg 38, 981 07 Abisko, Sweden
[e] Department of Forest Ecology and Management, Swedish University of Agricultural Sciences, SE-90183 Umeå, Sweden
[f] School of Forest Sciences, University of Eastern Finland, Joensuu, Finland

ARTICLE INFO

Editor: Marie Weiss

Keywords:
Peatland
Moisture estimation
Hyperspectral
Multispectral
Continuous wavelet transform
EnMAP

ABSTRACT

Northern peatlands are critical carbon stores that are highly sensitive to hydrological conditions. Changes in these conditions, driven by climate change and land-use modifications, can even shift peatlands from carbon sinks to sources. Consequently, effective management of both natural and restored peatlands requires monitoring of hydrological parameters such as soil moisture. Recently launched hyperspectral satellites like EnMAP provide new capabilities for this monitoring through enhanced spectral resolution.

This study presents a novel framework for estimating peatland soil moisture content by applying Continuous Wavelet Transform (CWT) with real-valued Morlet wavelet to EnMAP satellite data. We evaluated the performance of CWT-processed data against original EnMAP bands, multispectral Sentinel-2 data, and spectral moisture indices across nine peatland sites spanning hemiboreal, boreal, sub-Arctic, and Arctic zones in Finland, Sweden, and Estonia. The CWT-processed EnMAP model achieved the highest predictive accuracy (R^2 = 0.67, RMSE = 14.02%), followed by original EnMAP bands (R^2 = 0.50, RMSE = 17.23%), while Sentinel-2 bands showed substantially lower performance (R^2 = 0.32, RMSE = 20.09%) despite having finer spatial resolution. These results suggest that spectral resolution outweighs spatial resolution for peatland soil moisture estimation. Spectral moisture indices performed poorly with both satellite sensors (R^2 = 0.00–0.17), demonstrating the limitations of single band combinations compared to full spectral approaches. While spatial mismatch between ground measurements and satellite pixel size, along with limited hyperspectral data availability, constrained this study, our results demonstrate the potential of hyperspectral satellite data and CWT for peatland soil moisture monitoring. Future validation across diverse peatland types and restoration conditions would further strengthen these findings.

1. Introduction

Northern peatlands (>23°N) function as persistent sinks of atmospheric carbon dioxide (CO_2), storing approximately 415 gigatons of carbon in peat soils (Hugelius et al., 2020). Peatlands' ability to sequester and store carbon is dependent on water availability, which regulates vegetation productivity and decomposition rates of organic matter (Frolking et al., 2010; Zhong et al., 2020). However, these ecosystems and their carbon storage functions are under threat from climate change and direct land-use modifications, such as agriculture, forestry, and peat extraction (Harris et al., 2022). In northern regions, climate change impacts are especially pronounced, with warming rates projected to surpass the global average (IPCC, 2021). Changes in temperature and precipitation trends could even transform peatlands from carbon sinks to sources (Frolking et al., 2011; Qiu et al., 2022). This risk is particularly critical in permafrost peatlands, where thawing ground is already causing significant greenhouse gas emissions (Ramage et al., 2024). Similarly, land-use changes cause substantial carbon emissions, with affected sites continuing to release CO_2 even decades after the initial disturbance (Nugent et al., 2019).

* Corresponding author.
E-mail address: susanna.karlqvist@aalto.fi (S. Karlqvist).

https://doi.org/10.1016/j.rse.2026.115367
Received 10 December 2025; Received in revised form 12 February 2026; Accepted 11 March 2026
Available online 17 March 2026

Given these threats, protecting intact peatlands and restoring degraded ones are crucial for climate change mitigation (Leifeld and Menichetti, 2018). Restoration efforts typically focus on rewetting drained peatlands, as stable waterlogged conditions help restore carbon storage capacity and enable ecosystem recovery (Loisel and Gallego-Sala, 2022; Li et al., 2025). Although rewetting can initially increase methane (CH_4) emissions, the net climate effect is beneficial as reductions in CO_2 emissions help transition peatlands back into carbon sinks over time (Humpenöder et al., 2020).

Effective management of both natural and restored peatlands requires monitoring their hydrological conditions (Minasny et al., 2023), which can be assessed through near-surface soil moisture or water-table position. Traditional ground-based measurements, however, are restricted to small spatial scales, as they are labor-intensive and, even when automated, limited to point measurements. Furthermore, peatlands are often located in remote, inaccessible regions, making field campaigns time-consuming and logistically challenging (Ghazaryan et al., 2024). Remote sensing offers several advantages over these field studies, especially in terms of cost-effectiveness, integration over larger spatial scales, and accessibility to remote locations. Additionally, many satellite datasets are freely available and have regular resampling intervals, making them ideal for monitoring temporal hydrological changes. Despite these advantages, existing satellite-derived soil moisture products often perform poorly in peatlands (Burgin et al., 2017) and have coarse spatial resolutions ($\geq$ 1 km) (Das et al., 2019) that fail to capture the fragmented nature of peatlands or the spatial variability in hydrological conditions within peatland complexes. These limitations highlight the need to develop more accurate soil moisture estimation techniques specifically for peatlands.

Studies estimating peatland hydrological conditions through satellite remote sensing have primarily relied on multispectral and synthetic aperture radar (SAR) data (Burdun et al., 2023; Ghazaryan et al., 2024; Reddin et al., 2025; Ikkala et al., 2026). However, the recent launch of hyperspectral satellites, such as Environmental Mapping and Analysis Program (EnMAP) (Storch et al., 2023) and PRecursore IperSpettrale della Missione Applicativa (PRISMA) (Cogliati et al., 2021), will now also enable the use of hyperspectral data, which capture finer spectral details across hundreds of narrow bands. Upcoming missions, such as Surface Biology and Geology (SBG) (Thompson et al., 2020) and the Copernicus Hyperspectral Imaging Mission for the Environment (CHIME) (Nieke et al., 2023) are expected to further enhance hyperspectral data availability and temporal coverage.

Among spectral analysis techniques, spectral indices have been predominant for extracting biophysical parameters from both hyper- and multispectral data. These indices have also been applied to estimate peatland hydrology (Harris and Bryant, 2009; Meingast et al., 2014; Lees et al., 2020; Giese et al., 2025). However, spectral indices demonstrate inconsistent performance across diverse peatland types and struggle with accurately detecting low moisture conditions (Räsänen et al., 2022; Isoaho et al., 2024; Karlqvist et al., 2025). Consequently, exploring alternative spectral methods is needed to improve the accuracy and robustness of hydrological monitoring.

One promising alternative to spectral indices is the Continuous Wavelet Transform (CWT), a signal processing technique that decomposes hyperspectral signatures into a multiscale representation, enabling the simultaneous analysis of narrow absorption features and broader spectral patterns (Rivard et al., 2008). CWT has successfully estimated biophysical parameters from close-range spectral measurements of plant leaves (Blackburn, 2007; Cheng et al., 2011; Harrison et al., 2018; Yang et al., 2025) and peatland vegetation (Kalacska et al., 2015; Banskota et al., 2017; Karlqvist et al., 2024; Karlqvist et al., 2025). CWT has also been applied to reconstructed time series of spectral indices from multispectral satellite data (Qiu et al., 2014; Zhao et al., 2019). However, the direct application of CWT as a spectral processing technique for hyperspectral satellite data remains unexplored.

This study aims to evaluate how well hyperspectral satellite data can estimate peatland hydrological conditions using near-surface soil moisture. We present a novel framework that applies CWT to EnMAP satellite data. To assess its performance, we compare CWT with original EnMAP bands, hyperspectral moisture indices, and multispectral data from Sentinel-2. Our analysis covers nine peatland sites in Finland, Sweden, and Estonia, representing hemiboreal, boreal, sub-Arctic, and Arctic peatlands. To our knowledge, this is the first study using EnMAP data to estimate surface soil moisture in northern peatlands. Specifically, we address the following questions: (i) Does applying CWT to hyperspectral satellite data improve peatland soil moisture estimation compared to approaches using original spectral bands and moisture indices? (ii) How does hyperspectral EnMAP data compare to multispectral Sentinel-2 data for peatland soil moisture estimation?

2. Materials and methods

2.1. Study sites

Data were collected from nine peatland sites in Estonia, Sweden, and Finland (Fig. 1). The study sites included one Estonian site: Luhasoo; two sites in Sweden: Abisko-Stordalen and Degerö (detailed site description in Noumonvi et al., 2023); and six sites in Finland: Halssiaapa, Kaamanen (Aurela et al., 2001), Lompolojänkkä (Lohila et al., 2010), Patvinsuo (Turunen et al., 2002), Siikaneva (Korrensalo et al., 2025), and Tervalamminsuo. A summary of site characteristics is provided in Table 1.

2.2. Moisture measurements

Near-surface soil moisture was measured at each site within the active surface soil layer using either manual or automatic methods, except at Halssiaapa, where both methods were used. Across all sites, a plot was defined as a sampling location that provided one soil moisture value for analysis. However, the approach for deriving this value differed between manual and automatic sites.

Manual measurements at Luhasoo, Patvinsuo, and Halssiaapa were conducted as part of a broader field campaign by Salko et al. (2024a). At these manual sites, each plot consisted of three adjacent 1 m $\times$ 1 m subplots spaced approximately 2 m apart (center-to-center). Plot coordinates were recorded at the center of the middle subplot. Within each subplot, soil volumetric water content was measured at five points (four corners and center) from 0 to 6 cm depth using a ML3 Thetakit sensor set to “organic mode” (Delta-T Devices Ltd, 2017). Salko et al. (2024a) analyzed these measurements for outliers, which were identified as data points that deviated from the theoretical relationship between the sensors' voltage and percentage outputs, likely due to transcription errors during manual data recording. However, no outliers were identified in the data used in this study. The final soil moisture value for each plot at manual sites was calculated as the arithmetic mean of all measurements across the three subplots.

Temporal differences existed between manual data collection and satellite acquisitions: two days at Luhasoo, up to three days at Patvinsuo, and up to seven days at Halssiaapa (Table 2). To account for potential changes in soil moisture during these intervals, meteorological data from nearby weather stations were examined for the period between field measurements and satellite overpasses. For Luhasoo, data from the Tuulmäe weather station, located approximately 10 km east of the peatland site, indicated 4 mm cumulative precipitation during the two-day interval (ILM, 2025). For Patvinsuo, the Ilomantsi Pötsönvaara station (~17 km southeast) recorded 1 mm of precipitation over the three-day period (FMI, 2025a). At Halssiaapa, the Sodankylä Tähtelä station (~1 km west) registered 3 mm of precipitation during the seven-day interval (FMI, 2025a). Given the relatively low precipitation, substantial changes in surface soil moisture were considered unlikely, and data from all three sites were included in the analysis.

At automatic measurement sites, near-surface soil moisture was

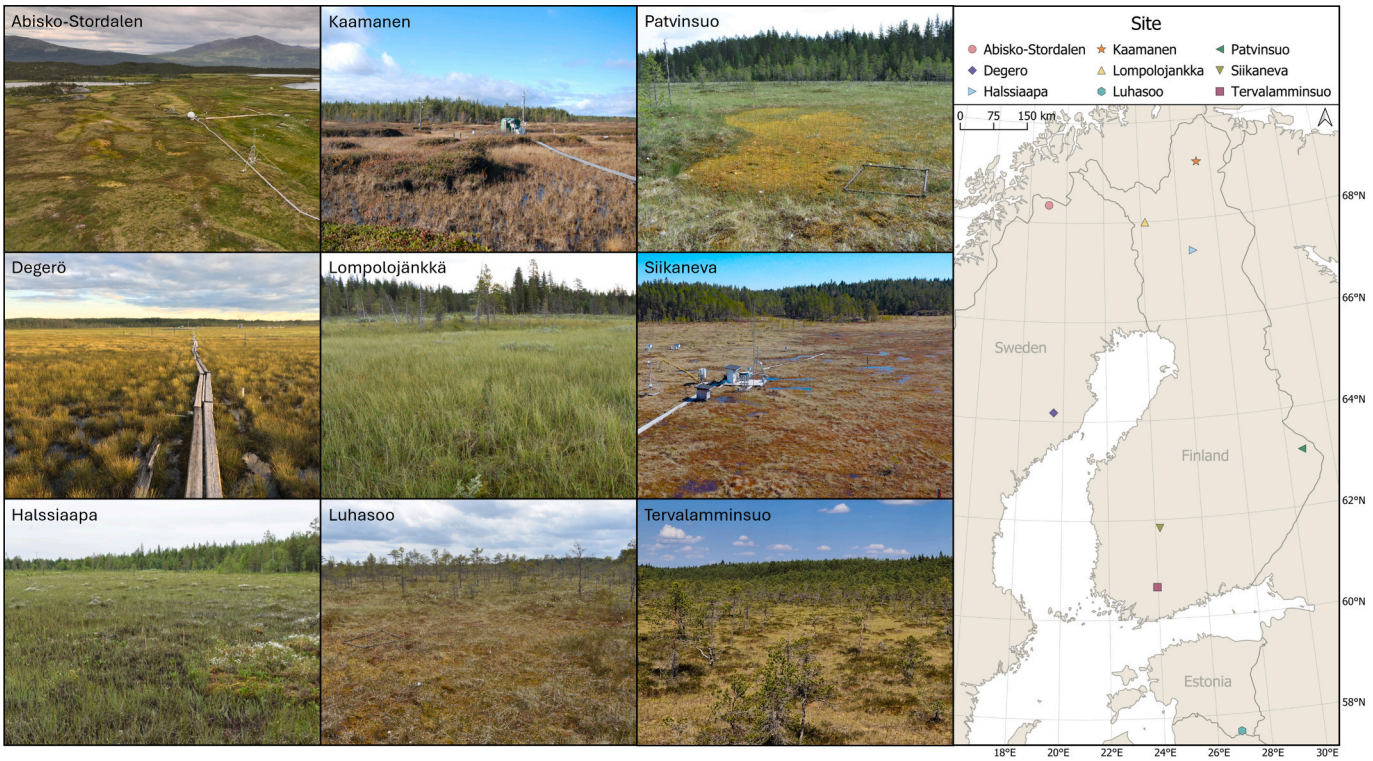

Fig. 1. Map of the peatland sites used in this study, with field photos. Photo credits: Niklas Rakos (Abisko-Stordalen) and Pasi Jalkanen (Siikaneva).

recorded continuously using automatic sensor-logger systems. These sensors were installed with their body positioned above the peat surface and measurement prongs extending vertically into the peat, ensuring consistent measurement of the surface layer. For most automatic sites, each plot's soil moisture value corresponded to a single sensor reading. However, at Kaamanen, the plot's moisture value was calculated as the mean of three individual sensor readings located within a 10 m radius. Kaamanen measurements were collected from the dry string, wet flark and the moss surface between them. At Tervalamminsuo, soil moisture was measured in a hollow, while at Abisko-Stordalen, all measurements were collected on permafrost peat plateaus. In Siikaneva, moisture was measured in the lawn, flark, and hummock levels. Other sites included both wetter and drier measurement locations. Measurement depths also varied due to different instrumentation and site-specific characteristics: 5 cm at Siikaneva, Degerö, Halssiaapa, and Lompolojänkkä; 7.5 cm at Tervalamminsuo and Kaamanen; and 10 cm at Abisko-Stordalen. Although 5 cm measurements were also available at Abisko-Stordalen, we utilized the 10 cm depth to account for the palsa structure. However, the difference between these measurements was minimal (< 2%). Overall, variations in measurement depth were assumed to have an insignificant impact and were therefore considered negligible.

High-frequency automatic measurements enabled the use of soil moisture data from the nearest half-hour interval corresponding to the satellite overpass time. Consequently, different soil moisture values were used for EnMAP and Sentinel-2 data, depending on image acquisition times. Nevertheless, most images were acquired on the same or consecutive days (Table 2), resulting in minimal differences in ground reference values (< 0.25%). Exceptions were the images acquired for Degerö in August 2025 and Lompolojänkkä in September 2025, where temporal gaps between satellite acquisitions were larger. Additionally, a data logger malfunction at Lompolojänkkä during this period meant that soil moisture values had to be obtained from the nearest available measurements: 27.8.2025 for EnMAP and 10.9.2025 for Sentinel-2.

2.3. Satellite data

We used temporally coincident hyperspectral data from the EnMAP mission and multispectral data from the Copernicus Sentinel-2 mission. From both sources, we applied level-2A orthorectified and atmospherically corrected bottom-of-atmosphere reflectance, which is hereafter referred to as reflectance. The specific acquisition dates for EnMAP and Sentinel-2 images are detailed in Table 2.

The EnMAP hyperspectral imager, developed by the German Aerospace Center (DLR), provides data in 224 spectral bands from 418.2 to 2445.5 nm at a 30 m spatial resolution. The sensor's spectral sampling varies between 4.7 nm and 8.2 nm in the Visible Near-Infrared (VNIR; 418.2–993 nm) and between 7.5 nm and 12 nm in the Short-Wave Infrared (SWIR; 902.2–2445.5 nm), excluding the sampling gaps caused by strong atmospheric absorption (Storch et al., 2023). EnMAP imagery was downloaded from the EOWEB Geoportal (https://eoweb.dlr.de/egp/). The L2A products were processed using land-mode atmospheric correction and bilinear interpolation, with no cirrus or haze removal, no band interpolation applied, and no automatic ozone column.

Sentinel-2 data were acquired from the Sentinel-2 A, Sentinel-2B, and Sentinel-2C satellites, each equipped with the Multi-Spectral Instrument (ESA, 2025). We used all L2A bands with a spatial resolution of either 10 or 20 m. These bands and their central wavelengths are: B2 at 490 nm, B3 at 560 nm, B4 at 665 nm, B5 at 705 nm, B6 at 740 nm, B7 at 783 nm, B8 at 842 nm, B8a at 865 nm, B11 at 1610 nm, and B12 at 2190 nm. The data was downloaded via the Copernicus Data Space Ecosystem (https://browser.dataspace.copernicus.eu/).

2.4. Data processing

We used QGIS software (version 3.40) to evaluate the quality of all satellite images and to extract reflectance data. Specifically, pixels intersecting with the soil moisture measurement plots and their immediate neighbors were manually inspected to confirm they were free from clouds or cloud shadows. Additionally, the georeferencing of each

Table 1
Summary of the study sites including geographic coordinates (WGS84), elevation above sea level (a.s.l.), mean annual temperature (MAT), mean annual precipitation (MAP), site type, microtopography, and dominant vegetation. MAT and MAP are for the period 1991–2020 (reference: Finnish sites (Jokinen et al., 2021), Luhasoo (ILM, 2025), Abisko-Stordalen (SMHI, 2025), and Degerö (Noumonvi et al., 2023)).

Site	Location (coordinates, m a.s.l.)	MAT (°C)	MAP (mm)	Site type	Microtopography	Dominant Vegetation
Abisko-Stordalen	68°21′N, 19°03′E, 360	0.4	350	Arctic discontinuous permafrost peatland	Ombrotrophic peat plateaus underlain by permafrost, bog and fen areas with subsiding thaw ponds	Dry: *Sphagnum* spp., *Polytrichum* spp., *Betula nana*, *Empetrum nigrum*, *Vaccinium* spp., *Rubus chamaemorus* Wet: *Eriophorum* spp., *Sphagnum* spp.
Degerö	64°11′N, 19°33′E, 270	3.0	645	Boreal oligotrophic minerogenic mire	Lawns, carpets and occasional hummocks	*S. balticum*, *S. majus*, *S. lindbergii*, *Eriophorum vaginatum*, *Trichophorum cespitosum*, *Vaccinium oxycoccos*, *Andromeda polifolia*
Halssiaapa	67°22′N, 26°39′E, 180	0.3	543	Sub-Arctic open eutrophic fen	Wet flarks, intermediate lawns, raised strings and treed strings	Flarks: *Eriophorum* spp., *Scheuchzeria palustris* Lawns: *Carex* and *Sphagnum* spp. Strings: *Sphagnum* spp., *Betula nana*, *Andromeda polifolia*, *Vaccinium oxycoccos* and *Pinus* spp.
Kaamanen	69°08′N, 27°16′E, 155	0.3	485	Sub-Arctic mesotrophic aapa mire	Raised strings and wet flarks	String tops: *Empetrum nigrum*, *Rhododendron tomentosum*, *Vaccinium* spp., *Rubus chamaemorus* Margins: *Betula nana*, *Sphagnum* spp. Flarks: *Scorpidium* spp., *Carex* spp., *Trichophorum* spp.
Lompolojänkkä	67°60′N, 24°13′E, 269	−0.6	532	Sub-Arctic open minerotrophic fen	Flarks and lawns	Wet: *Carex rostrata*, *C. chordorrhiza*, *C. magellanica*, *C. lasiocarpa*, *Menyanthes trifoliata*, *Equisetum fluviatile*, *S. riparium*, *S. fallax* Dry: *Betula nana*, *Salix lapponum*, *Andromeda polifolia*, *Vaccinium oxycoccos*, *S. russowii*, *S. angustifolium*
Luhasoo	57°39′N, 26°54′E, 145	6.5	658	Hemiboreal ombrotrophic bog with transitional mire and fen elements	Treed and open hummocks, lawns, and hummock-hollow-pools	Ombrotrophic: *Andromeda polifolia*, *Vaccinium oxycoccos*, *Eriophorum vaginatum*, *S. fuscum*, *S. angustifolium* Transitional: *Carex* spp., *Phragmites australis*, *Menyanthes trifoliata*, *Pinus sylvestris*
Patvinsuo	63°09′N, 30°38′E, 150	3.0	616	Boreal mixed aapa-bog complex	Lawns, ombrotrophic hummocks, and treed hummocks	Ombrotrophic: *Empetrum nigrum*, *Calluna vulgaris*, *Chamaedaphne calyculata*, *V. uliginosum*, *V. microcarpum*, *Eriophorum vaginatum*, *S. fuscum*, *S. angustifolium* Minerotrophic: *Carex pauciflora*, *S. papillosum* Tree species: *Pinus sylvestris*
Siikaneva	61°50′N, 24°12′E, 164	4.1	690	Boreal open oligotrophic fen	Lawns, flarks and small hummocks	Lawns: *Sphagnum papillosum* and *S. balticum* Flarks: *S. fallax* and *S. majus* High lawns and low hummocks: *S. angustifolium* and *S. magellanicum* Vascular plants: Dwarf shrubs dominate drier microforms (high lawns and low hummocks), while sedges *Carex lasiocarpa*, *C. rostrata*, and the herb *Scheuchzeria palustris* dominate wetter microforms
Tervalamminsuo	60°39′N, 23°58′E, 117	5.3	640	Boreal ombrotrophic raised bog	Ridge-hollow pine bog	*Calluna vulgaris*, *Andromeda polifolia*, *Eriophorum vaginatum*, *Rubus chamaemorus*, *Empetrum nigrum*, *Rhododendron tomentosum*, *Vaccinium uliginosum*, *S. fuscum*, *S. rubellum*, *S. balticum*, *Pinus sylvestris*

satellite image was evaluated against regional orthoimages. When spatial misalignment was detected, the offset between the satellite image and the orthoimage was calculated, cross-verified against other satellite images of the region and used to adjust soil moisture plot coordinates accordingly. This correction was necessary for two EnMAP (Lompolojänkkä, 19.7.2025; Abisko-Stordalen, 31.7.2023) and one Sentinel-2 (Abisko-Stordalen, 27.8.2023) images.

Reflectance values were extracted from both EnMAP and Sentinel-2 images using the EnMAP-Box plugin (version 3.16.3) within QGIS. The objective was to isolate the spectra corresponding to the exact pixel that intersected with each soil moisture measurement location. However, direct point-based extraction posed challenges, as many plots were located near pixel boundaries of one or both sensor grids. For these boundary cases, single-pixel extraction risked capturing incomplete or unrepresentative spectral information, particularly given that peatland surfaces exhibit hummock-hollow microtopography that creates soil moisture variability at sub-pixel scales. Additionally, despite evaluating the georeferencing of each satellite image against regional orthoimages, residual geolocation uncertainties could result in slight spatial misalignments between the pixel grid and ground positions. To address these issues, a 5-m buffer was applied around each measurement plot. The buffer size was deliberately smaller than the pixel size of both sensors (10–20 m for Sentinel-2; 30 m for EnMAP) to limit extraction to the pixel containing the measurement plot and its immediate neighbors, which were most likely to represent the measurement location. Each buffer was overlaid separately on the EnMAP and Sentinel-2 pixel grids, and intersecting pixels were extracted independently, preserving each sensor's native grid geometry. This approach allowed the inclusion of adjacent pixels when the measurement plot fell near pixel boundaries, while avoiding the incorporation of more distant pixels that would be less representative of the plot conditions.

The extracted spectra were processed in Python, where all EnMAP files were consolidated into one data frame and all Sentinel-2 files into another. During this process, spectral profiles were converted into wavelength-specific reflectance values, while preserving all associated metadata. To create a single representative spectrum for each plot where the buffer intersected multiple pixels, reflectance values from each intersecting pixel were aggregated using a weighted average. The weight for each pixel was the proportion of the total buffer area that intersected with that pixel, ensuring that pixels with larger intersection

Table 2
Satellite image acquisition dates, number of field plots per site used for the analysis, time of the soil moisture collection, sensors used, and reference to the soil moisture data. Imaging time refers to the exact time of the satellite overpass for both EnMAP and Sentinel-2 images.

Site	Date of EnMAP data	Date of Sentinel-2 data	Number of field plots	Time of moisture collection	Moisture measurement sensor	Reference of moisture data
Abisko-Stordalen	31.7.2023	31.7.2023	2	Imaging time	Campbell SoilVue10	(Lundin et al., 2025)
	26.8.2023	27.8.2023	2	Imaging time		
Degerö	7.9.2024	7.9.2024	4	Imaging time	Meter ECH2O EC-5 and 10HS	(Nilsson et al., 2025)
	17.8.2025	13.8.2025	3	Imaging time		
Halssiaapa manual	28.6.2023	29.6.2023	10	4.7.2023	Delta-T ML3 Thetakit	(Salko et al., 2024b)
Halssiaapa automatic	28.6.2023	29.6.2023	3	Imaging time	Campbell CS655	(FMI, 2025b)
Kaamanen	21.8.2023	21.8.2023	1	Imaging time	Delta-T ML2x Thetaprobe	Not published
Lompolojänkkä	28.6.2024	27.6.2024	3	Imaging time	Delta-T ML3 Thetaprobe	(Lohila et al., 2025)
	6.9.2024	7.9.2024	3	Imaging time		
	19.7.2025	19.7.2025	3	Imaging time		
	1.9.2025	11.9.2025	3	EnMAP: 27.8.2025 Sentinel-2: 10.9.2025		
Luhasoo	19.5.2023	19.5.2023	7	17.5.2023	Delta-T ML3 Thetakit	Not published
Patvinsuo	27.6.2023	28.6.2023	7	27 or 30.6.2023	Delta-T ML3 Thetakit	(Salko et al., 2024b)
Siikaneva	20.8.2023	20.8.2023	5	Imaging time	Delta-T PR2 profile probe	(Tuittila et al., 2025)
	8.5.2024	9.5.2024	5	Imaging time		
	5.6.2024	5.6.2024	5	Imaging time		
Tervalamminsuo	21.6.2024	20.6.2024	1	Imaging time	Delta-T ML2x Thetaprobe	Not published

areas had proportionally greater influence on the final reflectance value.

Several harmonization steps were applied to ensure data consistency. For EnMAP data, to account for a spectral band update on 5.7.2023 (EnMAP, 2023), only wavelengths common to all images were retained.

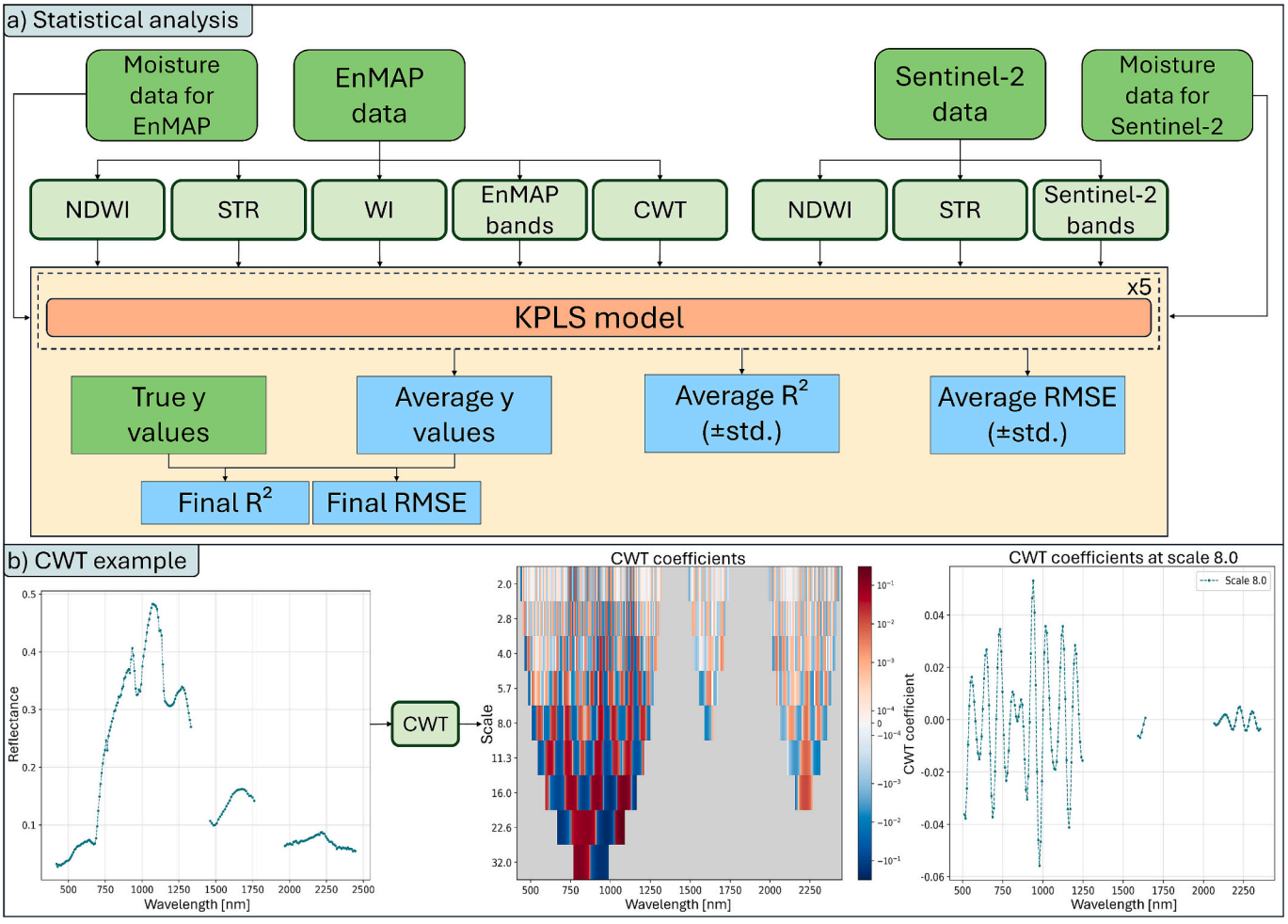

Fig. 2. a) Illustration of the statistical analysis framework. b) Example of how Continuous Wavelet Transform (CWT) changes reflectance values to CWT coefficients. NDWI stands for Normalized Difference Water Index, STR is the SWIR Transformed Reflectance, and WI is the Water Index. True y values refer to the original moisture data for either EnMAP or Sentinel-2 dataset depending on the model. KPLS refers to Kernel Partial Least Squares, R^2 is the coefficient of determination, RMSE is the Root Mean Square Error, and std. is the standard deviation.

Furthermore, in the overlapping spectral region (approximately 902–993 nm), where both VNIR and SWIR instruments collect data, only VNIR bands were used. For Sentinel-2 data, the EnMAP-Box plugin did not incorporate the new 2022 processing baseline 04.00 (ESA, 2025) that shifts Level-2A products by a radiometric offset. Therefore, the offset was manually corrected.

Following these processing steps, the initial datasets for both EnMAP and Sentinel-2 comprised 74 plots. An additional quality control procedure was then applied to identify plots unsuitable for satellite-based analysis. Manual review of orthoimages, with field verification, identified seven unsuitable plots where dense tree canopy or open water overlapped with satellite pixels. After removing these plots, 67 plots remained for analysis.

2.5. Data analyses

2.5.1. Overview of analyses

In this study, we analyzed the use of EnMAP and Sentinel-2 data for peatland soil moisture estimation, using spectral moisture indices (Section 2.5.2), full EnMAP spectra, full Sentinel-2 spectra, and CWT-processed EnMAP spectra (Section 2.5.3). The used spectral moisture indices and the CWT technique are detailed in the following sections, while the full spectra approach utilized all available reflectance values from the respective sensors as model parameters. All approaches were evaluated using Kernel Partial Least Squares (KPLS) regression with repeated nested 5-fold cross-validation (Section 2.5.3), implemented in Python. A summary of the analyses is shown in Fig. 2a.

Additionally, we compared the EnMAP and Sentinel-2 spectra collected on the same day or within one day of each other. Spectra from plots where the EnMAP and Sentinel-2 images were taken more than one day apart were excluded from this comparison. However, these plots were retained in the statistical analyses, as all models were trained exclusively using either EnMAP or Sentinel-2 data.

2.5.2. Spectral moisture indices

Spectral moisture indices have been widely used for estimating soil moisture conditions from reflectance data due to their simplicity and computational efficiency. While several studies have demonstrated strong correlations between moisture indices and peatland soil moisture (Letendre et al., 2008; Harris and Bryant, 2009; Meingast et al., 2014), others have, more recently, reported declining performance when applied to measurements from multiple sites (Lees et al., 2020; Karlqvist et al., 2025). However, to provide a broader assessment of spectral methods using hyperspectral and multispectral satellite data, we evaluated the performance of several moisture indices.

From our previous research in northern peatlands (Karlqvist et al., 2025), we selected the two best-performing indices: the Water Index (WI) and the SWIR Transformed Reflectance (STR). The WI is a hyperspectral index, while the STR can be applied to both hyper- and multispectral data. In addition to these indices, we included the Normalized Difference Water Index (NDWI), which is also applicable to both hyper- and multispectral data. Consequently, our analysis included three indices for the EnMAP data and two for the Sentinel-2 data. The equations for all indices are presented in Table 3.

2.5.3. Continuous wavelet transform

CWT transforms hyperspectral data into coefficients by scaling and shifting a mother wavelet ($\psi(\lambda)$) (Bruce et al., 2001) as:

$$\psi_{a,b}(\lambda) = \frac{1}{\sqrt{a}}\psi\left(\frac{\lambda - b}{a}\right) \quad (1)$$

Where λ signifies the wavelength, while a and b are positive real numbers representing scaling and shifting factors, respectively. The scaling factor controls the width of the mother wavelet, determining how many spectral bands contribute to each coefficient (Rivard et al., 2008), while the shifting factor translates the wavelet along the spectral range (Blackburn, 2007). To ensure that the CWT coefficients are comparable across scales and different spectra, the mean reflectance spectrum must be subtracted from each wavelength band (Rivard et al., 2008). The CWT of a reflectance spectrum $f(\lambda)$ is then calculated as (Bruce et al., 2001):

$$W_f(ab) = \langle f\psi_{a,b}\rangle = \int_{-\infty}^{+\infty} f(\lambda)\psi_{a,b}(\lambda)d\lambda \quad (2)$$

The resulting CWT coefficients $W_f(a,b)$, form a two-dimensional matrix called a scalogram, where one dimension represents scales and other the position on the wavelength axis. This position is directly comparable to the corresponding wavelength of the original spectrum (Rivard et al., 2008).

For the mother wavelet ($\psi(\lambda)$), we selected the real valued Morlet wavelet as it outperformed other tested wavelets, including the Mexican hat wavelet, and Gaussian derivatives from 1 to 8. The real Morlet wavelet is calculated as:

$$\psi(\lambda) = \exp\left(-\frac{\lambda^2}{2}\right)(1 - \lambda^2) \quad (3)$$

While CWT can be performed on discrete signals, such as spectral data, it requires continuous parameter values. This requirement means that the spectral bands must have a uniform sampling interval (Torrence and Compo, 1998). However, EnMAP data does not have uniform sampling and contains large gaps caused by atmospheric water absorption bands between the VNIR (418.2–1330.9 nm), SWIR1 (1461.1–1759.5 nm), and SWIR2 (1967.7–2445.5 nm) regions. To address this non-uniformity, we developed a segmented CWT workflow in which each spectral region was interpolated to even spacing and transformed independently. The reflectance data were resampled onto an evenly spaced wavelength grid using the Piecewise Cubic Hermite Interpolating Polynomial (PCHIP) method. The target spacing for this new grid matched the average original EnMAP band spacing within each segment, resulting in actual achieved spacings of 7.668 nm (VNIR), 11.005 nm (SWIR1), and 8.380 nm (SWIR2). The CWT was then computed on each interpolated segment.

Due to the finite data length, edge effects can render coefficients at the beginning and the end of the spectrum unreliable (Torrence and Compo, 1998). To handle this, a Cone of Influence (COI) was calculated for each segment's scalogram. For the Morlet wavelet, COI was defined as $\sqrt{2} \times a$ (Torrence and Compo, 1998). All coefficients within the COI were masked and excluded from further analysis, ensuring findings

Table 3
Spectral moisture indices used in this study and their equations. For EnMAP indices, R denotes the reflectance at the specified wavelength. For Sentinel-2 indices, B corresponds to the reflectance at that band.

EnMAP indices		
Index	Equation	Reference
Normalized Difference Water Index (NDWI)	$\frac{R_{550.7} - R_{847.9}}{R_{550.7} + R_{847.9}}$	McFeeters (1996)
SWIR Transformed Reflectance (STR)	$\frac{(1 - R_{1609})^2}{2 \times R_{1609}}$	Sadeghi et al. (2015)
Water Index (WI)	$\frac{R_{903.9}}{R_{968.9}}$	Peñuelas et al. (1997)

Sentinel-2 indices		
Index	Equation	Reference
Normalized Difference Water Index (NDWI)	$\frac{B3 - B8}{B3 + B8}$	McFeeters (1996)
SWIR Transformed Reflectance (STR)	$\frac{(1 - B11)^2}{2 \times B11}$	Sadeghi et al. (2015)

relied solely on valid coefficients unbiased by edge effects. Finally, the valid, unmasked CWT coefficients from the three segments were concatenated into a single coherent scalogram for the full spectral range.

Scales are often written as powers of two for convenience, with most CWT spectral studies applying integral powers of two (i.e., 2^1, 2^2, etc.) (Cheng et al., 2011; Banskota et al., 2017; Karlqvist et al., 2025; Yang et al., 2025). However, we decided to use fractional powers of two as scales as suggested by Torrence and Compo (1998). According to Torrence and Compo (1998), the smallest scale should also be at least twice the sampling interval. Therefore, we calculated the scales (a) as:

$$a = 2 \times 2^j, j = 0, 0.5, 1, \ldots, 4 \quad (4)$$

The interval for j values was set to 0.5. This selection yielded 9 scales, providing an adequately smooth representation of wavelet power. A smaller value could be used for higher resolution, while larger one would reduce the computational requirements. The maximum scale was limited to 32 ($j = 4$), as larger scales would cause the COI to cover the entire spectrum. The CWT was performed using the PyWavelets library (Lee et al., 2019), and an example of CWT for a single spectrum is shown in Fig. 2b.

2.5.4. Statistical modelling

For statistical modelling, we applied the KPLS algorithm as implemented by Rosipal and Trejo (2001), using the non-linear iterative partial least squares in feature space. We selected KPLS because it extends the linear Partial Least Squares (PLS) model into a higher-dimensional feature space, allowing it to capture possible non-linear relationships between predictors and the target variable, while remaining mathematically simple (Allegrini and Olivieri, 2023). PLS-based models are especially useful when working with highly collinear predictors, such as spectral data, or when the number of predictors exceeds the number of observations (Wold et al., 2001), as is the case with our data.

We used the Gaussian kernel for feature mapping, which was previously effective with peatland spectral data (Karlqvist et al., 2025). The Gaussian kernel is calculated by:

$$K = \exp\left(-\gamma \parallel x_i - x_j \parallel^2\right) \quad (5)$$

Here, γ is a hyperparameter that impacts the model's robustness and sensitivity (Wang et al., 2015). For training data x_i and x_j are both input vectors from the training set, while for test data, they are vectors from the test set and training set, respectively. The second hyperparameter for KPLS is the number of latent variables.

To build a robust model with optimized hyperparameters, we employed a nested five-fold cross-validation framework repeated five times to ensure stability. The outer loop partitioned the data into five folds using stratified sampling to ensure a balanced distribution of the target variable. Given the environmental heterogeneity and uneven sampling across sites, the stratified approach was chosen to assess the model performance across a broad range of soil moisture conditions. Within each fold, the reflectance data were standardized using only the training data to prevent information leakage and then applied to transform the corresponding test set. For each training set in this outer loop, an inner five-fold cross-validation grid search was conducted to identify the optimal hyperparameter combination, selecting the parameters with the lowest average Root Mean Squared Error (RMSE) across the folds.

For the optimal hyperparameters, the number of latent variables was chosen from the range 1–20, while γ values were selected from logarithmic ranges within 10^{-10} to 10^1, with multipliers from 1 to 9.9 in steps of 0.1 for each power of ten. If γ values approached the lower bound ($\approx 1 \times 10^{-10}$), the kernel projection approximated a linear transformation, suggesting that linear PLS would have been sufficient (Allegrini and Olivieri, 2023). However, preliminary analyses showed that PLS and KPLS yielded equivalent performance when all γ values approached 1×10^{-10}. Therefore, KPLS was applied uniformly across all models for consistency. Models were all γ values approached 1×10^{-10} were the original EnMAP bands, and the hyperspectral NDWI models.

Model performance was assessed in two ways (Fig. 2a). First, for reporting, we calculated the average coefficient of determination (R^2) and RMSE values from the results of the five independent repeats. Second, the final performance metrics used for plotting were derived by first averaging the predictions for each sample across all five repeats and then calculating the aggregated predictions against the actual measured values.

3. Results

3.1. Spectral characteristics of EnMAP and Sentinel 2 data

We visualized the spectral variation in the study sites using field plots where satellite images were acquired on the same day or within one day of each other with both continuous hyperspectral (EnMAP) data and discrete multispectral (Sentinel-2) data (Fig. 3). Despite the significant disparity in spectral resolution, the bands common to both sensors exhibited comparable reflectance values and consistent inter-site variability. However, the continuous nature of EnMAP data enabled more detailed temporal characterization of surface properties and enhanced differentiation between sites.

Overall, the spectral signatures were distinct across sites, despite all images being acquired during the growing season. For instance, the Arctic Kaamanen plot had lower reflectance values than the other sites, particularly in the visible region and beyond 960 nm. Conversely, the boreal Tervalamminsuo plot showed the highest reflectance in the SWIR 2 region. All other sites included multiple plots with varying degrees of within-site variability, though the overall spectral shape remained fairly consistent within each site.

The greatest variability was observed at the boreal Siikaneva site, with a mean coefficient of variation (CV) of 0.17 across the measured EnMAP spectrum. Although the Siikaneva measurement points were in close proximity, the spectra were collected from multiple images distributed across the growing season. Siikaneva was also the only multi-image site that included data from the start of the growing season. The sub-Arctic Halssiaapa plots displayed the second-highest mean CV (0.14). Notably, variation among 13 plots from a single Halssiaapa image exceeded that observed at other sites with multiple acquisition dates. These included Arctic Abisko-Stordalen, sub-Arctic Lompolojänkkä, and boreal Degerö, which exhibited mean CVs of 0.13, 0.10, and 0.10, respectively. This reduced variability could be attributed to the tighter spacing of soil moisture measurement points and the closer timing of satellite images. However, the boreal Patvinsuo and hemi-boreal Luhasoo sites (mean CVs of 0.10 and 0.07, respectively), which featured spatially dispersed measurements, also exhibited lower within-site variability. These results suggest that the Patvinsuo and Luhasoo sites have more homogeneous environmental conditions across their respective plots compared to Halssiaapa.

3.2. Prediction of soil moisture using hyperspectral and multispectral indices

The spectral moisture indices performed poorly for soil moisture detection with both EnMAP and Sentinel-2 data (Table 4). For hyperspectral EnMAP data, the best results were obtained with WI (average $R^2 = 0.16$ and RMSE = 22.38%). For multispectral Sentinel-2 data, NDWI achieved the best results (average $R^2 = 0.17$ and RMSE = 22.20%). Notably, all models based on spectral indices exhibited limited ability to predict low (0–20%) and high (90–100%) moisture content. This limitation suggests that standard spectral indices may not effectively capture the subtle variations in soil moisture present in complex peatland surfaces.

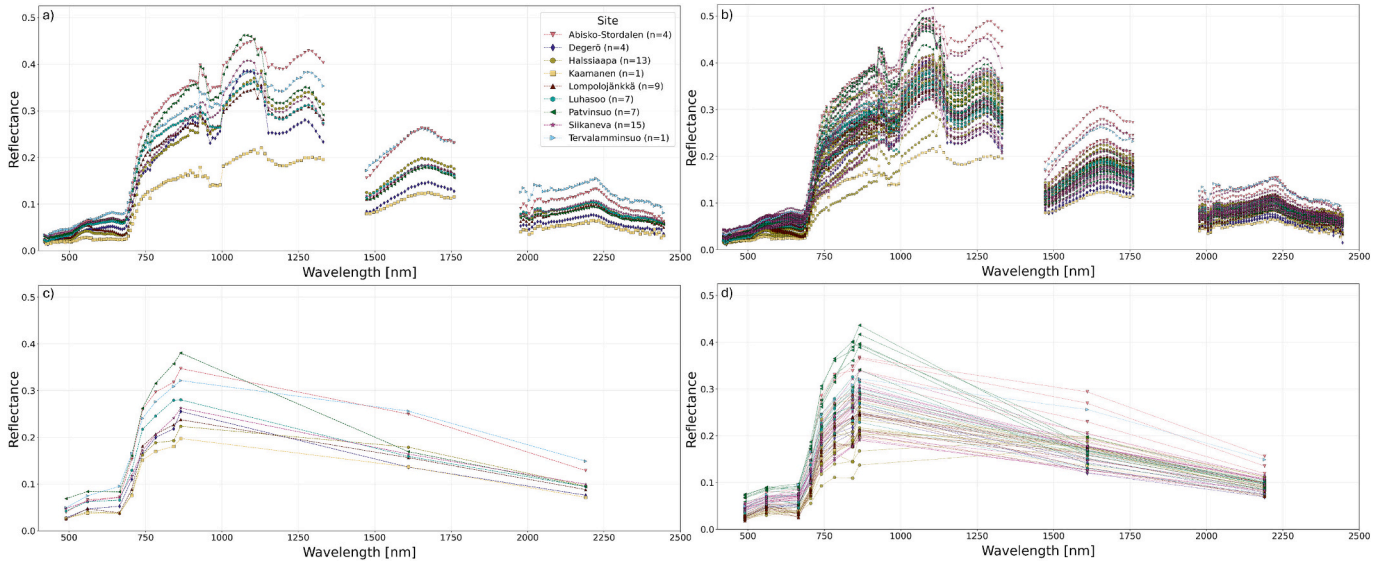

Fig. 3. Comparison of EnMAP (a-b) and Sentinel-2 (c-d) reflectance spectra from plots where satellite images were acquired on the same day or within one day of each other. Subplots a and c display mean reflectance spectra per site, while b and d show spectra of each individual plot derived from a, b) continuous EnMAP data and c, d) central wavelengths of Sentinel-2 bands. Reflectance values are shown with symbols and symbols of the same spectrum are connected with a dotted line for visualization. The legend indicates the number of plots (n) per site included in the comparison.

Table 4
The coefficient of determination (R^2), the root mean square error (RMSE), and their standard deviations (std) for models using a hyperspectral or multispectral spectral moisture index as a predictor. The results are the average of five model repeats.

Predictor	R^2 (± std.)	RMSE (± std.) %
EnMAP indices		
NDWI	0.08 (0.01)	23.37 (0.11)
STR	0.03 (0.12)	23.98 (1.45)
WI	0.16 (0.01)	22.38 (0.11)
Sentinel-2 indices		
NDWI	0.17 (0.03)	22.20 (0.36)
STR	0.00 (0.05)	24.39 (0.59)

3.3. Prediction of soil moisture using EnMAP bands, CWT-processed spectra and Sentinel-2 bands

The models applied to all EnMAP bands, CWT-processed EnMAP bands, and all Sentinel-2 bands demonstrated varying levels of predictive performance (Table 5; Fig. 4). The model utilizing original EnMAP spectral bands achieved moderate accuracy with an average R^2 of 0.50 and an RMSE of 17.23%, while the CWT model outperformed other methods with an average R^2 of 0.67 and an RMSE of 14.02%. In contrast, the model derived from Sentinel-2 bands demonstrated lower predictive accuracy, with an R^2 of 0.32 and an RMSE of 20.09%.

Visual inspection of prediction results (Fig. 4) suggests that prediction accuracy was highest for intermediate moisture values (40–80%), where data points are clustered closer to the 1:1 line. Conversely, increased scattering occurs at moisture extremes across all models, though this effect was most pronounced in the multispectral Sentinel-2 bands. The hyperspectral CWT and EnMAP models demonstrated more consistent performance across the moisture conditions.

Table 5
The coefficient of determination (R^2), the root mean square error (RMSE), and their standard deviations (std) for models using EnMAP bands, CWT-processed EnMAP bands, and Sentinel-2 bands. The results are the average of five model repeats.

Predictor	R^2 (± std.)	RMSE (± std.) %
EnMAP bands	0.50 (0.08)	17.23 (1.28)
EnMAP-CWT	0.67 (0.05)	14.02 (1.00)
Sentinel-2 bands	0.32 (0.05)	20.09 (0.69)

4. Discussion

4.1. CWT for peatland soil moisture estimation through hyperspectral satellite data

This research demonstrated that hyperspectral EnMAP satellite data can be used to predict surface soil moisture content in northern peatlands across hemiboreal to Arctic regions with relatively high accuracy. Specifically, applying CWT to the data yielded superior results compared to alternative techniques. Notably, this study represents the first application of CWT to satellite-based hyperspectral data, extending its use beyond previous close-range (Cheng et al., 2011; Kalacska et al., 2015; Banskota et al., 2017; Harrison et al., 2018) and airborne applications (Cheng et al., 2014). The superior performance of CWT can be attributed to its ability to decompose spectral signatures into multiscale representations (Rivard et al., 2008) that capture subtle moisture-related absorption features (Banskota et al., 2017). The robustness of CWT results across varying soil moisture values and diverse peatland types spanning multiple climatic zones further supports its potential as a generalizable method for peatland hydrological monitoring.

In this study, we selected a real-valued Morlet mother wavelet for CWT over other wavelets. This decision aligns with previous research by Kalacska et al. (2015), who similarly selected the Morlet wavelet over alternatives when predicting chlorophyll and nitrogen content from peatlands. The usefulness of the Morlet wavelet likely stems from its narrow spectral-space representation (Torrence and Compo, 1998), which enhances detection of narrow absorption features. Further analysis of other wavelets, including complex types, presents an opportunity to expand and refine the CWT method for peatland soil moisture estimation.

4.2. Comparison of hyperspectral and multispectral satellite data for peatland soil moisture estimation

Hyperspectral EnMAP data outperformed multispectral Sentinel-2

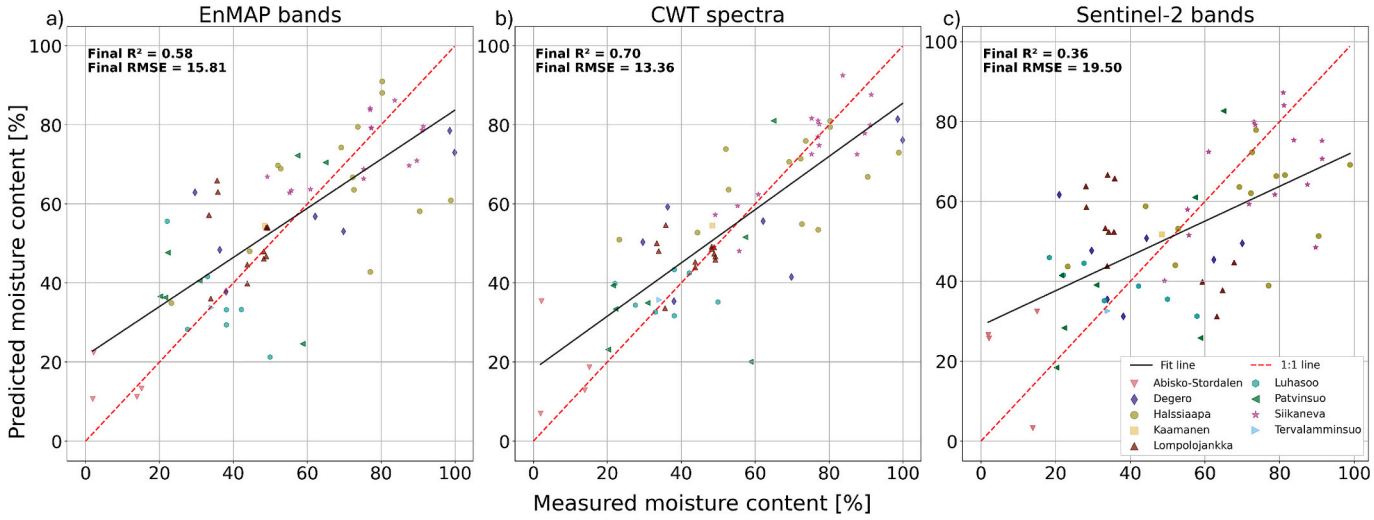

Fig. 4. Comparison of predicted versus measured relative moisture content using a) original EnMAP bands, b) CWT-processed EnMAP bands, and c) Sentinel-2 bands. The black solid line represents the line of best fit, while the red dashed line indicates the 1:1 relationship. Data points are colored by site. (For interpretation of the references to colour in this figure legend, the reader is referred to the web version of this article.)

data for peatland soil moisture estimation, with the CWT model achieving substantially higher predictive accuracy (R^2 = 0.67) compared to the Sentinel-2 band model (R^2 = 0.32). Even unprocessed EnMAP bands (R^2 = 0.50) demonstrated considerably better performance than Sentinel-2 model. This performance gap existed despite Sentinel-2's finer spatial resolution (10–20 m in Sentinel-2 vs. 30 m in EnMAP), suggesting that higher spectral resolution that can effectively capture water absorption features across different peatland types is more important than spatial resolution in peatland soil moisture estimation. Additionally, spectral moisture indices performed poorly with both sensors (R^2 = 0.00–0.17), indicating that indices relying on fixed band combinations are unreliable for large-scale monitoring across heterogeneous peatland environments.

While the models applying hyperspectral EnMAP data proved successful, predictive performance was not uniform across all hydrological conditions. Accuracy was highest at intermediate moisture levels, with increased scattering at the wet and dry extremes. This variance may be partly attributed to the data distribution, which contained a higher density of intermediate points, but it can also reflect site-specific characteristics such as peatland type and dominant vegetation. For instance, structural differences between *Sphagnum*-dominated bogs and sedge-rich fens likely influenced spectral response and model efficacy. Future research prioritizing site-specific validation is necessary to further explore these ecological relationships.

Our results extend previous findings on the utility of optical data for peatland soil moisture estimation from hyperspectral field studies and multispectral satellite studies (Ikkala et al., 2026) to hyperspectral satellite data. However, our multispectral results showed lower predictive performance compared to some previous studies estimating water table depth (Räsänen et al., 2022; Isoaho et al., 2024). This discrepancy is likely due to the distinction between surface soil moisture and water table depth. While these variables can be related, their relationship can weaken, especially during dry conditions or depending on ecological factors such as vegetation or peat depth (Moore et al., 2021). Furthermore, our study spanned a large latitudinal gradient, representing greater ecological variability than previous studies.

4.3. Study limitations and ways forward

While this study demonstrated the potential of hyperspectral satellite data for peatland soil moisture estimation, several limitations regarding data characteristics and methodological constraints must be acknowledged. These limitations include the spatial mismatch between the in-situ soil moisture measurements and the satellite pixel size, the temporal alignment of the data, data availability, and model constraints.

The EnMAP sensor has a spatial resolution of 30 m, whereas our ground-based measurements, derived from either clustered measurement points or single points per pixel, represented much smaller areas. This discrepancy introduced uncertainty, as these measurements may not capture soil moisture conditions across the entire pixel area. Furthermore, inconsistent sensor installation depths across datasets limited our ability to determine the specific depth at which soil moisture is most accurately estimated by satellite data. Future studies could mitigate these spatial and vertical constraints by employing more comprehensive field sampling designs with multi-level soil moisture sensors. However, given that such campaigns are labor-intensive with many field sites, one possibility is to leverage existing research infrastructures. Although these sites may not have been originally designed with remote sensing validation in mind, expanding them with more spatially distributed sensors could offer a cost-effective solution to bridge the scale gap. Alternatively, future hyperspectral satellite missions with finer spatial resolution would also help reduce the mismatch between pixel size and ground reference measurements.

Temporal alignment also presented challenges for a subset of the study sites. While field measurements for most sites coincided with satellite overpasses (Table 2), gaps of up to seven days occurred at three manually sampled locations. Although we examined meteorological data to confirm that significant precipitation events did not occur during these intervals, this approach cannot entirely rule out subtle changes in surface soil moisture. Furthermore, the analysis was constrained by the limited availability of cloud-free hyperspectral imagery from different parts of the growing season. This is a common challenge for studies using optical satellite data, particularly with newer missions like EnMAP, which have a lower revisit frequency than constellations like Sentinel-2. More frequent imaging would provide a more robust dataset, capturing a wider range of soil moisture conditions and phenological stages. However, we anticipate that this limitation will diminish as more data from current and future hyperspectral satellite missions become available.

The limited number of peatland plots and the uneven distribution of soil moisture values across them affect the model's generalizability. To ensure a balanced distribution of soil moisture values across the training and test sets, we employed a moisture-stratified cross-validation approach. This was necessary because soil moisture values were

unevenly distributed across our study sites, and a purely spatial cross-validation would have caused under-representation of soil moisture conditions across folds, requiring the model to extrapolate beyond the range of values in the training data (Roberts et al., 2017; Wadoux et al., 2021). However, this approach allowed plots from the same peatland to appear in both the training and test data, which ignored spatial autocorrelation. Consequently, our results may be optimistic, and the models' transferability to unseen locations remains unassessed (Roberts et al., 2017). Nevertheless, since our aim was to test the applicability of hyperspectral satellite data for peatland soil moisture estimation, the moisture stratified method was deemed appropriate. The broader applicability of our hyperspectral methods is supported by a field study that tested these approaches across hemiboreal to Arctic peatlands (Karlqvist et al., 2025), in which the CWT method, especially, demonstrated effectiveness also with spatial cross-validation.

Finally, this study was limited to mostly pristine peatlands. Future research could benefit from a geographically more expansive and diverse field reference dataset, covering a wider range of peatland types and restoration conditions with vegetation in different phenological stages. Such dataset would enable advanced statistical validation techniques, including spatial and temporal cross-validation, allowing for a more realistic assessment of model performance across new peatland sites. However, the logistical difficulties inherent to peatland fieldwork continue to limit the availability of such comprehensive reference datasets.

To further enhance estimation accuracy, future work could consider integrating multiple data sources. The fusion of hyperspectral data with multispectral, SAR, and meteorological data, alongside site-specific characteristics, could improve model robustness. SAR data is particularly valuable for its ability to penetrate cloud cover, ensuring consistent data collection regardless of weather conditions (Lees et al., 2021). Although SAR has generally shown lower predictive capability for peatland water table depth estimation than multispectral methods, it can be used to complement optical methods (Isoaho et al., 2024; Reddin et al., 2025), such as the hyperspectral methods demonstrated in this study. Therefore, while individual sources like SAR or in-situ measurements may not be strong predictors on their own, their integration with hyperspectral satellite data represents a promising avenue for more robust peatland monitoring.

5. Conclusion

This study demonstrated, for the first time, the applicability of hyperspectral satellite data for estimating near-surface soil moisture content across diverse northern peatland environments, spanning hemiboreal to Arctic conditions in three countries. Our findings showed that applying CWT to EnMAP hyperspectral data significantly improved soil moisture prediction accuracy compared to both original spectral bands and traditional spectral moisture indices. The comparison between hyperspectral and multispectral data revealed that spectral resolution is a more critical factor than spatial resolution for peatland soil moisture estimation. EnMAP data outperformed Sentinel-2 data despite its coarser spatial resolution, demonstrating the importance of high spectral resolution for detecting subtle water-absorption features essential for accurate soil moisture monitoring. Additionally, traditional spectral indices performed poorly with both sensors, indicating limited reliability for large-scale peatland monitoring across different peatland conditions. Future research should focus on expanding the reference dataset to include a wider variety of peatland types, including degraded and restored sites, and representing diverse phenological stages and hydrological conditions.

CRediT authorship contribution statement

Susanna Karlqvist: Writing – original draft, Visualization, Software, Methodology, Investigation, Formal analysis, Conceptualization. **Hermanni Aaltonen:** Writing – review & editing, Data curation. **Mika Aurela:** Writing – review & editing, Data curation. **Iuliia Burdun:** Writing – review & editing, Investigation, Data curation. **Mika Korkiakoski:** Writing – review & editing, Data curation. **Erik Lundin:** Writing – review & editing, Data curation. **Matthias Peichl:** Writing – review & editing, Data curation. **Sini-Selina Salko:** Writing – review & editing, Investigation, Data curation. **Eeva-Stiina Tuittila:** Writing – review & editing, Data curation. **Miina Rautiainen:** Writing – review & editing, Supervision, Project administration, Methodology, Funding acquisition, Conceptualization.

Declaration of competing interest

The authors declare that they have no known competing financial interests or personal relationships that could have appeared to influence the work reported in this paper.

Acknowledgements

We thank Metsähallitus and Riigimetsa Majandamise Keskus for allowing us to conduct research on their peatlands. We also thank Annalea Lohila of the ICOS Lompolojänkkä for providing data for this study. Funding: This study was mainly funded by the Research Council of Finland's Peatspec project (grant no. 3341963) and PeatResC Center of Excellence (grants no. 374133, 374130). Iuliia Burdun acknowledges FWO, which has co-financed the underlying research, Junior Postdoctoral Fellowship 12A5O24N. The Degerö and Abisko-Stordalen sites both contribute to the Swedish Infrastructure for Ecosystem Science (SITES) and are part of the Swedish Integrated Carbon Observation System (ICOS-Sweden) Research Infrastructure, with both infrastructures receiving funding from the Swedish Research Council (VR) and participating research institutions. The Siikaneva and Lompolojänkkä sites are part of the Finnish Integrated Carbon Observation System (ICOS-Finland) Research Infrastructure formed by University of Helsinki, Finnish Meteorological Institute and University of Eastern Finland. The Kaamanen, Tervalamminsuo and Halssiaapa (automatic measurements) sites are operated by Finnish Meteorological Institute.

Data statement

Links to the ground reference soil moisture measurements are listed in Table 2 of the article. All EnMAP data are available through the EnMAP data access portal at the following link: https://planning.enmap.org/. EnMAP data ©DLR [2023,2024,2025] All rights reserved. All Sentinel-2 data are available through the https://browser.dataspace.copernicus.eu/.

References

Allegrini, F., Olivieri, A.C., 2023. Two sides of the same coin: kernel partial least-squares (KPLS) for linear and non-linear multivariate calibration. A tutorial. Talanta Open 7. https://doi.org/10.1016/j.talo.2023.100235.

Aurela, M., Laurila, T., Tuovinen, J.-P., 2001. Seasonal CO2 balances of a subarctic mire. J. Geophys. Res. Atmos. 106. https://doi.org/10.1029/2000JD900481.

Banskota, A., Falkowski, M.J., Smith, A.M.S., Kane, E.S., Meingast, K.M., Bourgeau-Chavez, L.L., Miller, M.E., French, N.H., 2017. Continuous wavelet analysis for spectroscopic determination of subsurface moisture and water-table height in northern peatland ecosystems. IEEE Trans. Geosci. Remote Sens. 55, 1526–1536. https://doi.org/10.1109/tgrs.2016.2626460.

Blackburn, G.A., 2007. Wavelet decomposition of hyperspectral data: a novel approach to quantifying pigment concentrations in vegetation. Int. J. Remote Sens. 28. https://doi.org/10.1080/01431160600928625.

Bruce, L.M., Morgan, C., Larsen, S., 2001. Automated detection of subpixel hyperspectral targets with continuous and discrete wavelet transforms. IEEE Trans. Geosci. Remote Sens. 39, 2217–2226. https://doi.org/10.1109/36.957284.

Burdun, I., Bechtold, M., Aurela, M., De Lannoy, G., Desai, A.R., Humphreys, E., Kareksela, S., Komisarenko, V., Liimatainen, M., Marttila, H., Minkkinen, K., Nilsson, M.B., Ojanen, P., Salko, S.-S., Tuittila, E.-S., Uuemaa, E., Rautiainen, M., 2023. Hidden becomes clear: optical remote sensing of vegetation reveals water

table dynamics in northern peatlands. Remote Sens. Environ. 296. https://doi.org/10.1016/j.rse.2023.113736.
Burgin, M.S., Colliander, A., Njoku, E.G., Chan, S.K., Cabot, F., Kerr, Y.H., 2017. A comparative study of the SMAP passive soil moisture product with existing satellite-based soil moisture products. IEEE Trans. Geosci. Remote Sens. 55. https://doi.org/10.1109/TGRS.2017.2656859.
Cheng, T., Rivard, B., Sánchez-Azofeifa, A., 2011. Spectroscopic determination of leaf water content using continuous wavelet analysis. Remote Sens. Environ. 115, 659–670. https://doi.org/10.1016/j.rse.2010.11.001.
Cheng, T., Riaño, D., Ustin, S.L., 2014. Detecting diurnal and seasonal variation in canopy water content of nut tree orchards from airborne imaging spectroscopy data using continuous wavelet analysis. Remote Sens. Environ. 143, 39–53. https://doi.org/10.1016/j.rse.2013.11.018.
Cogliati, S., Sarti, F., Chiarantini, L., Cosi, M., Lorusso, R., Lopinto, E., Miglietta, F., Genesio, L., Guanter, L., Damm, A., Pérez-López, S., Scheffler, D., Tagliabue, G., Panigada, C., Rascher, U., Dowling, T.P.F., Giardino, C., Colombo, R., 2021. The PRISMA imaging spectroscopy mission: overview and first performance analysis. Remote Sens. Environ. 262. https://doi.org/10.1016/j.rse.2021.112499.
Das, N.N., Entekhabi, D., Dunbar, R.S., Chaubell, M.J., Colliander, A., Yueh, S., Jagdhuber, T., Chen, F., Crow, W., O'Neill, P.E., Walker, J.P., Berg, A., Bosch, D.D., Caldwell, T., Cosh, M.H., Collins, C.H., Lopez-Baeza, E., Thibeault, M., 2019. The SMAP and Copernicus sentinel 1A/B microwave active-passive high resolution surface soil moisture product. Remote Sens. Environ. 233. https://doi.org/10.1016/j.rse.2019.111380.
Delta-T Devices Ltd, 2017. User manual for the ML3 ThetaProbe. https://delta-t.co.uk/wp-content/uploads/2017/02/ML3-user-manual-version-2.1.pdf.
EnMAP, 2023. EnMAP SWIR Band Configuration Update. https://www.enmap.org/news/2023-07-04/ accessed 30.10.2025.
ESA, 2025. The Sentinel-2 SentiWiki. https://sentiwiki.copernicus.eu/web/sentinel-2 accessed 12.11.2025.
FMI, 2025a. Download Observations: Hourly Observations. https://www.ilmatieteenlaitos.fi/havaintojen-lataus accessed 16.9.2025.
FMI, 2025b. Observations at the Arctic space center, Sodankylä. Data from SUO0004 and SUO0005 stations at the peatland. Data available from 2015-06-27 to 2025-08-31. CC BY-NC 4.0.. https://litdb.fmi.fi/suo0004_data.php.
Frolking, S., Roulet, N.T., Tuittila, E., Bubier, J.L., Quillet, A., Talbot, J., Richard, P.J.H., 2010. A new model of Holocene peatland net primary production, decomposition, water balance, and peat accumulation. Earth Syst. Dynam. 1. https://doi.org/10.5194/esd-1-1-2010.
Frolking, S., Talbot, J., Jones, M.C., Treat, C.C., Kauffman, J.B., Tuittila, E.-S., Roulet, N., 2011. Peatlands in the earth's 21st century climate system. Environ. Rev. 19. https://doi.org/10.1139/a11-014.
Ghazaryan, G., Krupp, L., Seyfried, S., Landgraf, N., Nendel, C., 2024. Enhancing peatland monitoring through multisource remote sensing: optical and radar data applications. Int. J. Remote Sens. 45. https://doi.org/10.1080/01431161.2024.2387133.
Giese, L., Baumberger, M., Ludwig, M., Schneidereit, H., Sánchez, E., Robroek, B.J.M., Lamentowicz, M., Lehmann, J.R.K., Hölzel, N., Knorr, K.-H., Meyer, H., 2025. Recent trends in moisture conditions across European peatlands. Remote Sens. Appl.: Soc. Environ. 37. https://doi.org/10.1016/j.rsase.2024.101385.
Harris, A., Bryant, R.G., 2009. A multi-scale remote sensing approach for monitoring northern peatland hydrology: present possibilities and future challenges. J. Environ. Manag. 90, 2178–2188. https://doi.org/10.1016/j.jenvman.2007.06.025.
Harris, L.I., Richardson, K., Bona, K.A., Davidson, S.J., Finkelstein, S.A., Garneau, M., McLaughlin, J., Nwaishi, F., Olefeldt, D., Packalen, M., Roulet, N.T., Southee, F.M., Strack, M., Webster, K.L., Wilkinson, S.L., Ray, J.C., 2022. The essential carbon service provided by northern peatlands. Front. Ecol. Environ. 20. https://doi.org/10.1002/fee.2437.
Harrison, D., Rivard, B., Sánchez-Azofeifa, A., 2018. Classification of tree species based on longwave hyperspectral data from leaves, a case study for a tropical dry forest. Int. J. Appl. Earth Obs. Geoinf. 66. https://doi.org/10.1016/j.jag.2017.11.009.
Hugelius, G., Loisel, J., Chadburn, S., Jackson, R.B., Jones, M., MacDonald, G., Marushchak, M., Olefeldt, D., Packalen, M., Siewert, M.B., Treat, C., Turetsky, M., Voigt, C., Yu, Z., Hugelius, G., Loisel, J., Chadburn, S., Jackson, R.B., Jones, M., MacDonald, G., Marushchak, M., Olefeldt, D., Packalen, M., Siewert, M.B., Treat, C., Turetsky, M., Voigt, C., Yu, Z., 2020. Large stocks of peatland carbon and nitrogen are vulnerable to permafrost thaw. Proc. Natl. Acad. Sci. USA 117. https://doi.org/10.1073/pnas.1916387117.
Humpenöder, F., Karstens, K., Lotze-Campen, H., Leifeld, J., Menichetti, L., Barthelmes, A., Popp, A., Humpenöder, F., Karstens, K., Lotze-Campen, H., Leifeld, J., Menichetti, L., Barthelmes, A., Popp, A., 2020. Peatland protection and restoration are key for climate change mitigation. Environ. Res. Lett. 15. https://doi.org/10.1088/1748-9326/abae2a.
Ikkala, L., Wolff, F., Marttila, H., Ronkanen, A.-K., Alekseychik, P., Rana, P., Kohv, M., Tahvanainen, T., Tolvanen, A., Haghighi, A.T., Kumpula, T., Osborne, C., Ilmonen, J., Haapalehto, T., Kløve, B., Räsänen, A., 2026. Remote sensing applications for monitoring restoration outcomes in boreal forestry-drained peatlands - reviewed applications and future potential. Remote Sens. Environ. 333. https://doi.org/10.1016/j.rse.2025.115093.
ILM, 2025. Observation Data: Hourly Data. https://www.ilmateenistus.ee/ilm/ilmavaatlused/vaatlusandmed/?lang=en accessed 16.9.2025.
IPCC, 2021. Climate Change 2021: The Physical Science Basis. Contribution of Working Group I to the Sixth Assessment Report of the Intergovernmental Panel on Climate Change, p. 2391. https://doi.org/10.1017/9781009157896.
Isoaho, A., Ikkala, L., Päkkilä, L., Marttila, H., Kareksela, S., Räsänen, A., 2024. Multi-sensor satellite imagery reveals spatiotemporal changes in peatland water table after restoration. Remote Sens. Environ. 306. https://doi.org/10.1016/j.rse.2024.114144.
Jokinen, P., Pirinen, P., Kaukoranta, J.-P., Kangas, A., Alenius, P., Eriksson, P., Johansson, M., Wilkman, S., 2021. Tilastoja Suomen ilmastosta ja merestä 1991-2020. Finnish Meteorologica Institute. https://doi.org/10.35614/isbn.9789523361485.
Kalacska, M., Lalonde, M., Moore, T.R., 2015. Estimation of foliar chlorophyll and nitrogen content in an ombrotrophic bog from hyperspectral data: scaling from leaf to image. Remote Sens. Environ. 169. https://doi.org/10.1016/j.rse.2015.08.012.
Karlqvist, S., Burdun, I., Salko, S.-S., Juola, J., Rautiainen, M., 2024. Retrieval of moisture content of common Sphagnum peat moss species from hyperspectral and multispectral data. Remote Sens. Environ. 315. https://doi.org/10.1016/j.rse.2024.114415.
Karlqvist, S., Juola, J., Hovi, A., Salko, S.-S., Burdun, I., Rautiainen, M., 2025. Soil moisture content of northern peatlands from close-range spectral data. Eco. Inform. 92. https://doi.org/10.1016/j.ecoinf.2025.103466.
Korrensalo, A., Kettunen, J., Mehtätalo, L., Vanhatalo, J., Tuittila, E.-S., 2025. Detecting subtle change in species and trait composition and quantifying its uncertainty in a boreal peatland. J. Veg. Sci. 36. https://doi.org/10.1111/jvs.70025.
Lee, G., Gommers, R., Waselewski, F., Wohlfahrt, K., O'Leary, A., 2019. PyWavelets: a Python package for wavelet analysis. J. Open Source Softw. 4, 1237. https://doi.org/10.21105/joss.01237.
Lees, K.J., Artz, R.R.E., Khomik, M., Clark, J.M., Ritson, J., Hancock, M.H., Cowie, N.R., Quaife, T., 2020. Using spectral indices to estimate water content and GPP in Sphagnum Moss and other peatland vegetation. IEEE Trans. Geosci. Remote Sens. 58, 4547–4557. https://doi.org/10.1109/TGRS.2019.2961479.
Lees, K.J., Artz, R.R.E., Chandler, D., Aspinall, T., Boulton, C.A., Buxton, J., Cowie, N.R., Lenton, T.M., 2021. Using remote sensing to assess peatland resilience by estimating soil surface moisture and drought recovery. Sci. Total Environ. 761, 143312. https://doi.org/10.1016/j.scitotenv.2020.143312.
Leifeld, J., Menichetti, L., 2018. The underappreciated potential of peatlands in global climate change mitigation strategies. Nat. Commun. 9, 1. https://doi.org/10.1038/s41467-018-03406-6.
Letendre, J., Poulin, M., Rochefort, L., 2008. Sensitivity of spectral indices to CO2 fluxes for several plant communities in a Sphagnum-dominated peatland. Can. J. Remote. Sens. 34, S414–S425. https://doi.org/10.5589/m08-053.
Li, X., Wang, Y., Cai, J., Xu, G., Li, H., Dong, Y., Liu, S., Liu, Z., Wang, S., Xu, Z., 2025. Microbial mechanism of soil organic carbon content under waterlogging and water table fluctuation in drained peat soils. Eur. J. Soil Biol. 127. https://doi.org/10.1016/j.ejsobi.2025.103773.
Lohila, A., Aurela, M., Hatakka, J., Pihlatie, M., Minkkinen, K., Penttilä, T., Laurila, T., 2010. Responses of N2O fluxes to temperature, water table and N deposition in a northern boreal fen. Eur. J. Soil Sci. 61. https://doi.org/10.1111/j.1365-2389.2010.01265.x.
Lohila, A., Aaltonen, H., Aurela, M., Gerin, S., Hatakka, J., Mäkelä, T., Rainne, J., Tuovinen, J., Varjonen, S., 2025. ETC NRT Meteosens from Lompolojankka, 2024-11-04–2025-11-25. ICOS RI accessed 9.9.2025. https://hdl.handle.net/11676/09DKkahOMB6b1Bo7Ye583hM2.
Loisel, J., Gallego-Sala, A., 2022. Ecological resilience of restored peatlands to climate change. Commun. Earth Environ. 1, 3. https://doi.org/10.1038/s43247-022-00547-x.
Lundin, E., Crill, P., Grudd, H., Holst, J., Kristoffersson, A., Meire, A., Mölder, M., Rakos, N., 2025. ETC L2 Meteo from Abisko-Stordalen Palsa Bog, 2021-12-31–2024-12-31. ICOS RI accessed 9.9.2025. https://hdl.handle.net/11676/tRebcFed0c3xi5GvLdgROcEy.
McFeeters, S.K., 1996. The use of the Normalized Difference Water Index (NDWI) in the delineation of open water features. Int. J. Remote Sens. 17. https://doi.org/10.1080/01431169608948714.
Meingast, K.M., Falkowski, M.J., Kane, E.S., Potvin, L.R., Benscoter, B.W., Smith, A.M.S., Bourgeau-Chavez, L.L., Miller, M.E., 2014. Spectral detection of near-surface moisture content and water-table position in northern peatland ecosystems. Remote Sens. Environ. 152, 536–546. https://doi.org/10.1016/j.rse.2014.07.014.
Minasny, B., Adetsu, D.V., Aitkenhead, M., Artz, R.R.E., Baggaley, N., Barthelmes, A., Beucher, A., Caron, J., Conchedda, G., Connolly, J., Deragon, R., Evans, C., Fadnes, K., Fiantis, D., Gagkas, Z., Gilet, L., Gimona, A., Glatzel, S., Greve, M.H., Habib, W., Hergoualc'h, K., Hermansen, C., Kidd, D.B., Koganti, T., Kopansky, D., Large, D.J., Larmola, T., Lilly, A., Liu, H., Marcus, M., Middleton, M., Morrison, K., Petersen, R.J., Quaife, T., Rochefort, L., Rudiyanto, Toca, L., Tubiello, F.N., Weber, P.L., Weldon, S., Widyatmanti, W., Williamson, J., Zak, D., Minasny, B., Adetsu, D.V., Aitkenhead, M., Artz, R.R.E., Baggaley, N., Barthelmes, A., Beucher, A., Caron, J., Conchedda, G., Connolly, J., Deragon, R., Evans, C., Fadnes, K., Fiantis, D., Gagkas, Z., Gilet, L., Gimona, A., Glatzel, S., Greve, M.H., Habib, W., Hergoualc'h, K., Hermansen, C., Kidd, D.B., Koganti, T., Kopansky, D., Large, D.J., Larmola, T., Lilly, A., Liu, H., Marcus, M., Middleton, M., Morrison, K., Petersen, R.J., Quaife, T., Rochefort, L., Rudiyanto, Toca, L., Tubiello, F.N., Weber, P.L., Weldon, S., Widyatmanti, W., Williamson, J., Zak, D., 2023. Mapping and monitoring peatland conditions from global to field scale. Biogeochemistry 167, 4. https://doi.org/10.1007/s10533-023-01084-1.
Moore, P.A., Didemus, B.D., Furukawa, A.K., Waddington, J.M., 2021. Peat depth as a control on Sphagnum moisture stress during seasonal drought. Hydrol. Process. 35. https://doi.org/10.1002/hyp.14117.
Nieke, J., Despoisse, L., Gabriele, A., Weber, H., Strese, H., Ghasemi, N., Gascon, F., Alonso, K., Boccia, V., Tsonevska, B., Choukroun, P., Ottavianelli, G., Celesti, M., Nieke, J., Despoisse, L., Gabriele, A., Weber, H., Strese, H., Ghasemi, N., Gascon, F., Alonso, K., Boccia, V., Tsonevska, B., Choukroun, P., Ottavianelli, G., Celesti, M., 2023. The copernicus hyperspectral imaging mission for the environment (CHIME):

an overview of its mission, system and planning status. In: Sensors, Systems, and Next-Generation Satellites XXVII, p. 12729. https://doi.org/10.1117/12.2679977.
Nilsson, M., Peichl, M., Marklund, P., Boschetti, F., De Simon, G., Holst, J., Smith, P., Kozii, N., Dignam, R., Larmanou, E., Lofvenius, P., Molder, M., Andersson, T., Linderson, M., Lindgren, K., 2025. ETC L2 Meteo from Degero, 2018-12-31–2024-12-31. ICOS RI accessed 9.9.2025. https://hdl.handle.net/11676/mke1xZgsnTVrG1EAzyZT1Dxi.
Noumonvi, K.D., Ågren, A.M., Ratcliffe, J.L., Öquist, M.G., Ericson, L., Tong, C.H.M., Järveoja, J., Zhu, W., Osterwalder, S., Peng, H., Erefur, C., Bishop, K., Laudon, H., Nilsson, M.B., Peichl, M., 2023. Frontiers | The Kulbäcksliden Research Infrastructure: a unique setting for northern peatland studies. Front. Earth Sci. 11. https://doi.org/10.3389/feart.2023.1194749.
Nugent, K.A., Strachan, I.B., Roulet, N.T., Strack, M., Frolking, S., Helbig, M., Nugent, K.A., Strachan, I.B., Roulet, N.T., Strack, M., Frolking, S., Helbig, M., 2019. Prompt active restoration of peatlands substantially reduces climate impact. Environ. Res. Lett. 14. https://doi.org/10.1088/1748-9326/ab56e6.
Peñuelas, J., Pinol, J., Ogaya, R., Filella, I., 1997. Estimation of plant water concentration by the reflectance Water Index WI (R900/R970). Int. J. Remote Sens. 18, 2869–2875. https://doi.org/10.1080/014311697217396.
Qiu, B., Zhong, M., Tang, Z., Wang, C., 2014. A new methodology to map double-cropping croplands based on continuous wavelet transform. Int. J. Appl. Earth Obs. Geoinf. 26. https://doi.org/10.1016/j.jag.2013.05.016.
Qiu, C., Ciais, P., Zhu, D., Guenet, B., Chang, J., Chaudhary, N., Kleinen, T., Li, X., Müller, J., Xi, Y., Zhang, W., Ballantyne, A., Brewer, S.C., Brovkin, V., Charman, D.J., Gustafson, A., Gallego-Sala, A.V., Gasser, T., Holden, J., Joos, F., Westermann, S., 2022. A strong mitigation scenario maintains climate neutrality of northern peatlands. One Earth 5. https://doi.org/10.1016/j.oneear.2021.12.008.
Ramage, J., Kuhn, M., Virkkala, A.-M., Voigt, C., Marushchak, M.E., Bastos, A., Biasi, C., Canadell, J.G., Ciais, P., López-Blanco, E., Natali, S.M., Olefeldt, D., Potter, S., Poulter, B., Rogers, B.M., Schuur, E.A.G., Treat, C., Turetsky, M.R., Watts, J., Hugelius, G., 2024. The net GHG balance and budget of the permafrost region (2000−2020) from ecosystem flux upscaling. Glob. Biogeochem. Cycles 38. https://doi.org/10.1029/2023GB007953.
Räsänen, A., Tolvanen, A., Kareksela, S., 2022. Monitoring peatland water table depth with optical and radar satellite imagery. Int. J. Appl. Earth Obs. Geoinf. 112. https://doi.org/10.1016/j.jag.2022.102866.
Reddin, E., Hanafin, J., Tong, M., Gill, L., Healy, M.G., 2025. Modelling water table depth at rewetted peatlands with Sentinel-1 and Sentinel-2. Sci. Remote Sens. 11. https://doi.org/10.1016/j.srs.2025.100238.
Rivard, B., Feng, J., Gallie, A., Sanchez-Azofeifa, A., 2008. Continuous wavelets for the improved use of spectral libraries and hyperspectral data. Remote Sens. Environ. 112. https://doi.org/10.1016/j.rse.2008.01.016.
Roberts, D.R., Bahn, V., Ciuti, S., Boyce, M.S., Elith, J., Guillera-Arroita, G., Hauenstein, S., Lahoz-Monfort, J.J., Schröder, B., Thuiller, W., Warton, D.I., Wintle, B.A., Hartig, F., Dormann, C.F., 2017. Cross-validation strategies for data with temporal, spatial, hierarchical, or phylogenetic structure. Ecography 40. https://doi.org/10.1111/ecog.02881.
Rosipal, R., Trejo, L.J., 2001. Kernel partial least squares regression in reproducing kernel hilbert space. J. Mach. Learn. Res. 2, 97–123.
Sadeghi, M., Jones, S.B., Philpot, W.D., 2015. A linear physically-based model for remote sensing of soil moisture using short wave infrared bands. Remote Sens. Environ. 164, 66–76. https://doi.org/10.1016/j.rse.2015.04.007.
Salko, S.-S., Hovi, A., Burdun, I., Juola, J., Rautiainen, M., 2024a. Geographically extensive spectral library of peatland vegetation from 13 hemiboreal, boreal, sub-Arctic and Arctic peatland sites, 1. https://doi.org/10.17632/3866tj3w8v.1.
Salko, S.-S., Hovi, A., Burdun, I., Juola, J., Rautiainen, M., 2024b. Hyperspectral characterization of vegetation in hemiboreal, boreal and Arctic peatlands using a geographically extensive field dataset. Eco. Inform. 82. https://doi.org/10.1016/j.ecoinf.2024.102772.
SMHI, 2025. Ladda ner meteorologiska observationer, Abisko (188800): Lufttemperatur (dygn); Nederbördsmängd (dygt). https://www.smhi.se/data/hitta-data-for-en-plats/ladda-ner-vaderobservationer/precipitation24HourSum/188800 accessed 1.12.2025.
Storch, T., Honold, H.-P., Chabrillat, S., Habermeyer, M., Tucker, P., Brell, M., Ohndorf, A., Wirth, K., Betz, M., Kuchler, M., Mühle, H., Carmona, E., Baur, S., Mücke, M., Löw, S., Schulze, D., Zimmermann, S., Lenzen, C., Wiesner, S., Aida, S., Fischer, S., 2023. The EnMAP imaging spectroscopy mission towards operations. Remote Sens. Environ. 294. https://doi.org/10.1016/j.rse.2023.113632.
Thompson, D.R., Schimel, D.S., Poulter, B., Brosnan, I., Hook, S.J., Green, R.O., 2020. NASA's Surface Biology and Geology Concept Study: Status and Next Steps. IGARSS 2020–2020 IEEE International Geoscience and Remote Sensing Symposium. https://doi.org/10.1109/IGARSS39084.2020.9323295.
Torrence, C., Compo, G.P., 1998. A practical guide to wavelet analysis. Bull. Am. Meteorol. Soc. 79. https://doi.org/10.1175/1520-0477(1998)079.
Tuittila, E., Kolari, P., Korrensalo, A., Laakso, H., Levula, J., Mammarella, I., Matilainen, T., Männistö, E., Taipale, R., Vesala, T., 2025. ETC L2 Meteosens from Siikaneva, 2016-12-31–2025-09-30. ICOS RI accessed 9.9.2025. https://hdl.handle.net/11676/qi6fjv69bALqtbVEavVbl94a.
Turunen, J., Räty, A., Kuznetsov, O., Maksimov, A., Shevelin, P., Grabovik, S., Kimmo Tolonen, Pitkänen, A., Turunen, C., Meriläinen, J., Jungner, H., 2002. Development history of Patvinsuo mire. In: Nature Protection Publications of the Finnish Forest and Park Service, Series A, No 138. ISBN: 952-446-357-1.
Wadoux, A.M.J.-C., Heuvelink, G.B.M., Bruin, S.d., Brus, D.J., 2021. Spatial cross-validation is not the right way to evaluate map accuracy. Ecol. Model. 457. https://doi.org/10.1016/j.ecolmodel.2021.109692.
Wang, M., Yan, G., Fei, Z., 2015. Kernel PLS based prediction model construction and simulation on theoretical cases. Neurocomputing 165. https://doi.org/10.1016/j.neucom.2015.03.028.
Wold, S., Sjöström, M., Eriksson, L., 2001. PLS-regression: a basic tool of chemometrics. Chemom. Intell. Lab. Syst. 58. https://doi.org/10.1016/S0169-7439(01)00155-1.
Yang, N., Zhang, Z., Zhang, J., Yang, X., Liu, H., Chen, J., Ning, J., Sun, S., Shi, L., 2025. Accurate estimation of winter-wheat leaf water content using continuous wavelet transform-based hyperspectral combined with thermal infrared on a UAV platform. Eur. J. Agron. 168. https://doi.org/10.1016/j.eja.2025.127624.
Zhao, L., Li, Q., Zhang, Y., Wang, H., Du, X., Zhao, L., Li, Q., Zhang, Y., Wang, H., Du, X., 2019. Integrating the continuous wavelet transform and a convolutional neural network to identify vineyard using time series satellite images. Remote Sens. 11, 2641, 11. https://doi.org/10.3390/rs11222641.
Zhong, Y., Jiang, M., Middleton, B.A., 2020. Effects of water level alteration on carbon cycling in peatlands. Ecosyst. Health Sustain. 6. https://doi.org/10.1080/20964129.2020.1806113.